

# Integrated Sensing and Communication (ISAC) for Vehicles: Bistatic Radar with 5G-NR Signals

Nikhil K. Nataraja, Sudhanshu Sharma, Kamran Ali, Fan Bai, Rui Wang and Andreas F. Molisch

**Abstract**—As 5G [3GPP New Radio (NR)] deployments continue to expand, their use as an “opportunistic” bistatic radar sensing system that uses the *base station* (BS) as the *transmitter* (TX) and the *user equipment* (UE) as the *receiver* (RX) opens the possibility of a new sensing modality that does not need extra hardware, and thus efficiently realize ISAC. In particular, such 5G-based radar sensing can complement and enhance the existing monostatic radar in *advanced driver assistance systems* (ADAS) and future self-driving cars, e.g., for detecting *non-line-of-sight* (NLoS) objects. However, 5G-NR signals have been designed for communication purposes and, as per the 3GPP standard definition, they are neither continuous nor periodic in time and frequency. This then makes it challenging to create an efficient standards-compliant bistatic radar system. This paper describes a suite of methods for overcoming these obstacles. We first explore the different *reference signals* (RSs) defined in the NR standard, and then analyze how they can be best combined for radar purposes. We also present high-resolution parameter-based *serial interference cancellation* (SIC) to extract the scatterers in the delay-Doppler domain with better-than-Fourier resolution. The impacts of combined precoding and beamforming stipulated in the standard are also discussed in this paper. To demonstrate the validity of our approach, we simulate our results using synthetic channels and validate them with channel measurements.

**Index Terms**—5G, ISAC, signal of opportunity, bistatic radar, reference signals, irregular sampling, SIC, V2X

## I. INTRODUCTION

### A. Motivation

ADAS and similar systems that are based on real-time observations of the environment help in reducing accidents, driver stress, and environmental impacts of vehicles. A key component of such systems is radar, which is now ubiquitous in cars and trucks. The existing automotive radar sensors are *monostatic* radars operating at mmWave frequencies (typically 24, 77, or 140 GHz) and require a *line-of-sight* (LoS) to detect target vehicles/objects [2], [3]. However, there are numerous situations, e.g., highway merge, where LoS might not exist [4], [5]. As such, *bistatic* radar setups, where the TX and the RX are located separately, are more

suitable to use, particularly those where one of the nodes is significantly elevated, e.g., a BS or a road-side unit. Operating at lower frequency also results in greater robustness due to the reduced losses, and thus larger coverage. To avoid the high cost of building a specialized new infrastructure or UE hardware, using the existing systems to enable such radar operation is desirable. The obvious candidate to achieve such ISAC system is 5G, more precisely the 3GPP NR [6], [7]. Its *frequency range 1* (FR1) signals (sub 6 GHz) are now becoming ubiquitous and are expected to be used for both human communications and for *vehicle-to-vehicle* (V2V) and *vehicle-to-infrastructure* (V2I)—jointly called V2X—communications [8]; consequently, many cars will have integrated 5G modems. For radar purposes, the signals can be used either opportunistically, i.e., the vehicle exploits communication signals that are transmitted in any case, or the vehicle can trigger/request for “dummy” data to be transmitted to help the sensing; in the latter case, the benefit lies on exploiting the existing infrastructure. In either case, the radar system is similar to an *orthogonal frequency division multiplexing* (OFDM) radar [9] since OFDM is the modulation format of NR.

In contrast to the existing monostatic vehicular radar sensors, the TX (i.e., the BS) and the RX (i.e., the UE in the sensing car) are located separately. This then creates a bistatic setup [10].<sup>1</sup> The setup is different from—and more complex than—the “*downlink* (DL)” ISAC systems treated in the literature [11], which assumes that an *infrastructure node* senses the radar reflections of a DL signal. The bistatic nature of our setup alleviates the problem of self-interference, which is challenging for monostatic OFDM radar [12].

Using the channel estimates obtained from the OFDM signals, we can estimate the sensing parameters, e.g., delay and Doppler, of surrounding objects (particularly moving objects). However, standards-compliant NR signals have several peculiarities that create considerable difficulties for radar applications, unlike the signals designed from the bottom up for radar or ISAC. Challenges arise because i) NR is primarily optimized for communications with minimum always-on signals such that periodically repeated signals are scarce, ii) NR is based on an infrastructure-centric design, with almost all transmissions controlled by the BS. Although the UE may request transmissions from the BS, it cannot influence the signal structure or the transmission *bandwidth* (BW). Furthermore, NR transmissions can consist of a large variety of signal types; only some of them are suited to be

Copyright (c) 20xx IEEE. Personal use of this material is permitted. However, permission to use this material for any other purposes must be obtained from the IEEE by sending a request to pubs-permissions@ieee.org.

A part of this work has been presented at the IEEE GLOBECOM conference 2023 held in Kuala Lumpur, Malaysia from Dec 4-8 2023. The conference version can be found here, [1].

The work of Nikhil K. Nataraja, Sudhanshu Sharma, and Andreas F. Molisch was supported by a grant from General Motors (GM) R&D.

Nikhil K. Nataraja and Andreas F. Molisch are with the Dept. of ECE, University of Southern California (USC), Los Angeles, CA.

Kamran Ali and Fan Bai are with the GM R&D, Warren, MI.

Sudhanshu Sharma was with the Dept. of ECE, USC. He is now with Apple Inc., San Diego, CA.

Rui Wang was with the Dept. of ECE, USC. He is now with Google Inc., Mountain View, CA.

<sup>1</sup>To ease notation and due to its practical importance, we will discuss the V2I case; however, almost all of the discussion carries over to the V2V case as well.

primary sensing signals, some are not suited at all, while some can be used to augment the sensing performance. Thus, the first task in building a standards-compliant vehicular ISAC system is to identify the signal types suitable for sensing, and then analyze the trade-offs between the complexity in processing a particular type of signal and the performance improvement it provides. Once the signals are identified, they must be combined to estimate the sensing parameters robustly. Further challenges arise from the beamforming/precoding methodology in NR that distorts the signals beforehand such that the UE cannot separate the distortions from the propagation channel.

## B. Prior Work

Monostatic automotive radar using mmWave frequencies has been employed for a long time [2], [3] in applications such as adaptive cruise control, park assist, and lane-change assist. However, its application is based on the assumption that there is an LoS signal to the targets of interest, which might not be fulfilled. In [4] and [5], the authors discuss the difficulties of sensing in NLoS situations, and thus propose installing passive reflectors above the sidewalk to solve the problem; however, this requires precise placement and alignment of reflectors, which may not be able to illuminate all the objects.

ISAC systems provide *active* radar TXs that are elevated over the cars without any additional deployment cost. In recent years, researchers have been highly interested in ISAC, see the surveys [13]–[17]. The survey [11], focuses on integrating sensing/radar capability into existing communications networks, which is particularly relevant to the current work.

The issue of exploiting passive “signals of opportunity” for sensing is a problem closely related to ISAC. In this approach, there is no co-design between radar and communications; instead, on-air communication signals are exploited for passive sensing [18]–[20]. This approach has been widely explored, particularly for WiFi sensing, vital sign monitoring, and other healthcare services [21]–[24]. However, WiFi access points are limited to a small geographical area and may not be suitable for a vehicular environment. Other opportunistic signals used for passive sensing include the Digital Video Broadcast [25]. Recently, 5G signals have also been used in passive sensing [26]–[29] that processes the a priori known signals in the *passively* listening UE without setting up a communication link with the BS. However, due to the limited information on the precise structure of the transmitted signals (e.g., RS structure), passive systems achieve a degraded sensing performance compared to ISAC systems [30].

Traditional radar systems use either pulsed radar or *frequency-modulated continuous wave* (FMCW), whereas most ISAC or opportunistic systems employ OFDM signals. The principle of OFDM radar was first expounded in [9], which discussed the signal model and receiver processing, e.g., [31], [32], and Sec. II. One major difference between standard OFDM radar signals and standardized communications signals lies on the fact that the latter are transmitted only at specific locations (grid points) of the time-frequency plane.

Sensing with signals based on V2V communications standard IEEE 802.11p [33]–[35] (operating at 5.9 GHz) and IEEE 802.11ad [36]–[38] (at 60 GHz) has been explored.<sup>2</sup> However, these works are restricted to a monostatic setup and are based on standards that are losing popularity (802.11p) or have never been used in car manufacturing (802.11ad).

Radar based on the 3GPP LTE has been discussed in [39]–[41]. LTE has periodically repeated, uniformly spaced (in both time and frequency), and not-precoded *cell-specific RS* (CS-RS); hence, it avoids the challenges discussed at the end of Sec. I-A. Accordingly, radar sensing is much easier to solve in LTE than in NR. However, NR is now replacing LTE; thus, LTE-based radar systems are not future-proof.

5G-NR signals have also been used to perform sensing in [11], [30], [42]–[47]. In [43], all OFDM subcarriers and symbols are used for sensing, which is not possible in a multi-user system. In [11], the different RSs in 5G-NR that can be used for sensing are listed; however, the study does not comprehensively discuss their pros and cons. In [42], always-on signals, e.g., *synchronization signals* (SS), are used to perform radar sensing; however, these signals have relatively low periodicity and BW, and thus do not result in acceptable target identification performance. Although 5G *positioning RSs* (PRSs) are used in [45] to analyze the ambiguity function, the assumption is that the PRS is transmitted densely in the time domain, which may not always be feasible in real-time deployment scenarios. Meanwhile, [30], [46], [47] use *demodulation RSs* (DM-RSs) to perform sensing, but do not analyze the impact of their randomness on the sensing performance.

Traditional OFDM radar processing such as *discrete Fourier transform* (DFT), subspace methods such as MUSIC and ESPRIT, and compressive sensing techniques have to be adapted to process discontinuous measurements that would optimally combine RSs for sensing parameter estimation in standardized signals. In [44], 5G NR RSs are used to perform DFT sensing through linear interpolation to reconstruct the channel estimates for the entire grid; however, as discussed in Sec. III, linear interpolation is suboptimum, particularly in irregular grids. Further, the resolution obtained through the Fourier estimation used in [44] may not be sufficient for vehicular environments, particularly for sensing in FR1. Using nonuniform samples in subspace methods like ESPRIT [48] would have high computational complexity, and are thus not widely considered [11], [48]. compressive sensing techniques [30], [46] suffer from quantization problem and yield poor Doppler accuracy when encountered with limited RSs in the time domain [11].

In summary, the matter of using NR DL signals for radar has not been fully investigated. Issues such as how different RSs can be processed and combined, considering their possible irregular locations in the time-frequency plane, how the resolution of target location can be improved in the delay-Doppler domain, and how the problems associated with

<sup>2</sup>IEEE 802.11ad foresees both an OFDM and a single-carrier mode; the latter is thus not directly comparable to the situation of interest in this paper.

beamforming/precoding of DL signals can be resolved have yet to be studied.

### C. Contribution

We aim to close these gaps in this paper. In particular:

- We analyze the impact of the different types of RSs, along with their combinations and with payload data, on sensing performance, including aliasing, sidelobes, and noise sensitivity. We further investigate the effect of NR beamformers and precoders on sensing and suggest a scheme for identifying sub-bands using the same precoder settings that can be advantageously combined.
- We improve the resolution of the delay-Doppler estimation of targets through SIC techniques in multiple target scenarios.
- We demonstrate the validity and evaluate the performance of our proposed RS combinations and SIC algorithm based on V2V channel in an urban street.

We stress that this paper does not aim to develop new mathematics, but aims to combine the existing techniques to tackle a difficult but practically relevant problem.

### D. Organization of the Paper

Fig. 1 shows how the RX processing in an NR-based ISAC system works in relation to the sections of this paper. Although the system uses OFDM signaling (Sec. II), only a subset of these signals can be used, which needs to be appropriately selected according to the characteristics of the signals and sensing performance criteria set in Sec. III. Once the signals are selected, the target echoes are successively extracted through SIC (Sec. IV). Further, precoding in 5G-NR limits the possibility of using all RSs. We devise a method to find sub-bands that use the same precoder matrix (Sec. V). The target echoes can then be Doppler-filtered, and the delay-Doppler of the targets can be determined, as demonstrated - based on measurements - in Sec. VI.

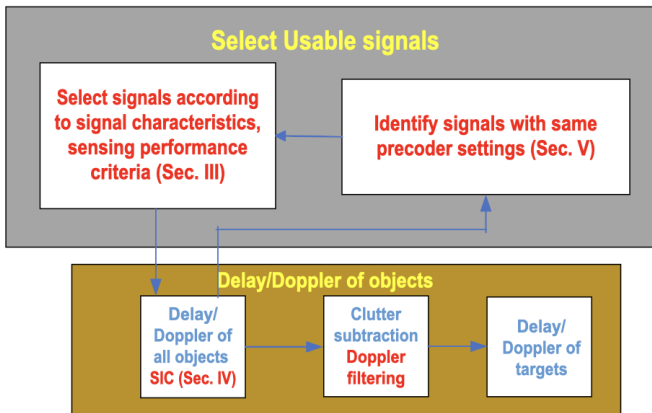


Fig. (1) High-level block diagram of receiver processing.

## II. FUNDAMENTALS OF BISTATIC OFDM RADAR

This paper deals with bistatic OFDM radars, where an OFDM waveform is transmitted and the standard OFDM channel estimation techniques [7, Ch. 15] allow the RX

to estimate the channel transfer function  $H_{k,l}$  at each subcarrier-symbol  $(k, l)$  pair of the OFDM grid. From this, the *spreading function* (SF)  $S(\tau, \nu)$  can be obtained as:

$$S(\tau, \nu) = \sum_{k=0}^{N_{sc}-1} \sum_{l=0}^{N_{sybm}-1} H_{k,l} e^{-j2\pi\nu l T_o} e^{j2\pi k \Delta f \tau} \quad (1)$$

where  $\tau$  is the time delay,  $\nu$  is the Doppler frequency,  $T_o$  is the symbol duration,  $\Delta f$  is the subcarrier spacing, and  $N_{sc}$  and  $N_{sybm}$  are the number of subcarriers and OFDM symbols, respectively, in the sensing signal. SF represents the received signal in the delay-Doppler plane, where the local maxima indicate the delay and Doppler corresponding to specific scatterers. This can be interpreted as the cross-ambiguity function of an ideal excitation signal between the TX and the RX signal. In traditional OFDM radar, the sensing signal is either on every grid point of the resource grid, i.e., every subcarrier/symbol pair, or on a sparser yet still regular grid. However, as detailed in Sec. III, the 5G RSs are placed nonuniformly and (possibly) randomly in the resource grid.

We consider here a setup where the BS transmits a single data stream to the UE, which may be beamformed and/or precoded, albeit the angular information of the *multipath components* (MPCs) and the beamformer and/or precoder settings used by the BS are unknown to the UE. Furthermore, we assume that the UE does not have RX angular information due to the lack of sufficient antennas or sufficiently accurate calibration. This allows us to model the system as an effective *single-input single-output* (SISO) system with one TX and one RX antenna. As such, let  $H_{k,l}$  denote the channel estimate at the  $k$ th subcarrier and  $l$ th OFDM symbol [32], and then:

$$H_{k,l} = \sum_{m=0}^{N_{MPC}-1} (b_{0m})_{k,l} e^{j2\pi\nu_m l T_o} e^{-j2\pi\tau_m k \Delta f} + (Z_1)_{k,l} \quad (2)$$

where  $N_{MPC}$  is the number of MPCs,  $\tau_m$  and  $\nu_m$  are the delay and Doppler of the  $m$ th MPC, respectively (which can be associated with a scatterer corresponding to a target or clutter), and  $(Z_1)_{k,l}$  is the additive noise (modeled as complex Gaussian). The notation  $(b_{0m})_{k,l}$  is the complex channel gain associated with the  $m$ th MPC including the gain from beamforming/precoding applied to the  $k$ th subcarrier and  $l$ th OFDM symbol. It has to be noted that *inter-carrier interference* (ICI) has been ignored in the above formulation. This assumption is realistic in vehicular environments with maximum Doppler of about 500 Hz (in sub-6 GHz carrier frequency) and a subcarrier spacing of 15 kHz.

The model assumes that the delay and Doppler of the scatterers are constant over the observation interval.<sup>3</sup> A potential problem in bistatic systems is the presence of independent TX and RX clocks, which leads to timing and frequency offsets. The existing techniques for correcting these offsets can be classified into three categories: (i) using a global reference clock, which can be realized with wired connections or via *Global Positioning System* (GPS). (ii) single-node-based solutions: most methods in that category are based on the

<sup>3</sup>The adaptive choice of time window in the case of changing delay/Doppler is a subject for future research.

fact that timing offset and carrier frequency offset are the same across multiple receive antennas if all the antennas use a common clock reference (e.g., *cross antenna cross correlation* (CACC) [49], [50] and its extensions, e.g., [51] and *cross antenna signal ratio* (CASR) [52], [53]) or estimating offsets based on strong static paths [54]. (iii) network-based solutions: 5G PRS signals can be employed in the standard to provide reliable localization. We have assumed, in this paper, that they are corrected using one of the above techniques. The key challenges in estimating the delay and Doppler are: i) the finite BW and observation period; ii) the channel estimates are available only at select  $k$  and  $l$  (grid locations of RSs); and iii) beamforming/precoding, which leads to different effective antenna patterns; thus,  $(b_{0m})$  may be different at different times/frequencies.

This work assumes that no beamforming is applied to any of the RSs, as is common in FR1. The following two sections assume that the BS does not precode the DM-RS, or the effects of the precoder can be inverted at the UE. The impact of precoding RSs is considered in Sec. V.

### III. USE OF 5G RSs IN RADAR SENSING

This section describes the characteristics of NR signals and the challenges in using them in ISAC systems. It then introduces a simple method for computing the SF for arbitrary samples in the time-frequency plane. It evaluates this function of different RSs and their combinations as to their suitability for target estimation in accordance with various criteria, i.e., periodicity, sidelobes and noise sensitivity.

#### A. Comparison with LTE

Radar detection is significantly more complex in NR than in LTE. In LTE, CS-RSs are transmitted periodically in the DL: in the *frequency division duplexing* (FDD) mode, they are placed on every sixth subcarrier in every slot's first and fourth symbol [7, Ch. 31].<sup>4</sup> Moreover, the CS-RSs extend over the whole system BW (per-carrier BW in LTE is  $\leq 20$  MHz) and are neither precoded nor beamformed. This allows a relatively straightforward processing for radar detection, which avoids the challenges in NR signals.

#### B. General Signal Structure of NR

In the time domain, NR transmissions are organized into frames of 10 ms, each divided into 10 equally sized subframes of 1 ms. A subframe is then divided into slots consisting of 14 OFDM symbols each. NR is designed to support BWs of up to 100 MHz for a single carrier in FR1.<sup>5</sup> A *resource element* (RE), consisting of one subcarrier during one OFDM symbol, is the smallest physical resource in NR. Furthermore, 12 contiguous REs in the frequency domain are called a *resource block* (RB). A maximum of 275 RBs (=3300 REs) can be used for a standard *physical downlink shared channel* (PDSCH) transmission. NR defines a *bandwidth part* (BWP) characterized by an active BW numerology (subcarrier spacing

and cyclic prefix) and a set of consecutive resource blocks in the numerology of the BWP.

There are two types of signals with known structure/data:

- **Synchronization signals (SS):** By receiving and analyzing the SS block, the UE can detect the band where the BS transmits and the timing of radio frames of the OFDM symbol boundary. Beam sweeping is also performed during synchronization. An SS block [*primary SS* (PSS) and *secondary SS* (SSS)] spans up to 127 subcarriers, extends up to 4 OFDM symbols in time, and has a repetition frequency of typically 20 ms, but which can be as large as 160 ms. In [42], these signals are used to perform sensing; however, their low BW ( $< 5$  MHz) and low periodicity make them unsuitable as a primary radar signal albeit they can help to augment other signals.
- **Reference signals (RSs):** These are predefined signals that occupy the specific REs within the resource grid. The main types of RSs are DM-RS, *phase tracking RS* (PT-RS), *channel state information RS* (CSI-RS), *tracking RS* (TRS), *sounding RS* (SRS), and PRS.

#### C. Impact of RS parameters on sensing

The various RSs may differ in their BW, *frequency domain location* (FDL), *time domain location* (TDL), *beamforming* (BF), and *precoding* (PR), see Table (I). The BW depends on the number of assigned subcarriers and on the subcarrier spacing; for FR1, this may range from 15 kHz to 60 kHz. Based on the elementary Fourier theory, a larger BW results in finer delay resolution; a longer observation interval similarly translates to finer Doppler resolution. When RSs are spaced regularly in the frequency domain, smaller spacings lead to a larger unambiguous delay; small spacings in the time domain result in larger unambiguous Doppler. Further, RSs in 5G differ in *time domain periodicity* (TDP): they can be periodic, aperiodic, and semi-periodic. They can also differ in their frequency domain periodicity.

#### D. Brief description of different RSs in 5G-NR

**CSI-RS** is designed to enable UEs to acquire DL *channel state information* (CSI). It spans the whole active BWP. The density in the frequency domain can be 3, 1, or 0.5 per RB.<sup>6</sup> The repetition interval in the time domain ranges from 4 to 640 slots. Although a UE can request for a CSI-RS to be transmitted, it is at the discretion of the BS to fulfill the request. CSI-RS is not precoded but (in FR1) may or may not be beamformed. **DM-RS** is meant for channel estimation at the RX as part of coherent demodulation and is present in RBs scheduled for data transmission. DM-RS can have either of two different mapping types (A and B) that determine the TDL and either of two different configuration types (1 and 2) that determine the FDL. Thus, the BS scheduler determines the TDL and FDL of DM-RSs. The BS precodes DM-RSs in either codebook-based or non-codebook-based [6] manner. Note that the DM-RS in RBs intended for other UEs cannot be

<sup>4</sup>The details of the location depend on the number of BS antennas and frame type.

<sup>5</sup>Carrier aggregation, i.e., simultaneous use of multiple component carriers, is allowed but will not be considered further in this paper.

<sup>6</sup>Density specifies the number of REs per RB populated with CSI-RS; 0.5 indicates that one CSI-RS RE is present in 2 RBs.

used for radar processing. **PT-RS** can be seen as an extension of DM-RS: it is denser in time but sparser in frequency (every second or fourth RB) and, if configured, occurs only in combination with DM-RS. Hence, it can be used only as a supplementary radar signal. Its intended purpose is for phase-noise compensation. **TRS** is a sparse RS for assisting the device in time- and frequency-tracking. It has various time periodicity settings ranging from 10 ms to 80 ms; due to the long periodicity, TRS is not well suited as a primary radar signal. **PRS** is a DL RS that supports positioning and extends throughout the system BW (more than the active BWP). In the frequency domain, the system configures a comb factor equal to 2, 4, 6, or 12 subcarriers. In the time domain, 2, 4, 6, or 12 OFDM symbols can be configured for one PRS resource. Signals from multiple sites are typically beamformed toward the UE to aid positioning using measurements from these sites, and muting interfering transmissions in adjacent cells improves reception quality. Receiving PRSs from multiple BSs can help to extract the position information of the UE accurately, but the relatively infrequent transmission of PRSs leads to poor Doppler estimation.

Most of these RSs exist over the active BWP only. Since the BW determines the delay resolution, the UE can improve delay resolution by requesting a large amount of dummy data from the BS, thus forcing an increased BW for the active BWP.

Henceforth, we focus on CSI-RS and DM-RS, as they are the most favorable for radar: CSI-RSs are regular and extend throughout the active BWP whereas DM-RSs can occur more frequently (along with PDSCH data). The other described RSs can be used to augment the sensing, but the additional performance benefit is small.

TABLE (I) List of RSs and their characteristics [6].

Signals	BW	FDL	TDL	TDP	BF/PR
SS	127 REs	contiguous	symbols 2-5	20 ms	Y/N
CSI-RS	active BWP	every 4th RE	symbol 0	4 slots	Y/N
DM-RS	intended RBs	every 2nd RE	symbol 2	random	Y/Y
PT-RS	intended RBs	every 2nd RB	dense	random	Y/Y
TRS	active BWP	every 4th RE	symbol 0	10 slots	Y/N
PRS	entire BW	every 6th RE	2 symbols	ms to sec	Y/N

#### E. Directly Computed Spreading Function (DCSF)

Since the RSs are available at irregularly spaced points in the resource grid, computing SF using (1) becomes challenging. Interpolating the transfer function to fill the whole time-frequency grid through simple methods, e.g., linear interpolation, are suboptimal for the delay and Doppler estimation, while the optimum reconstruction of band-limited signals [55] is complex and increases noise. The latter is especially problematic when interpolating using long sequences of missing values between samples and extrapolations. Accordingly, we consider using the DCSF as a simple but effective alternative. An estimate of the SF can be obtained using equation (1) by setting the channel estimates at non-RS locations to 0:

$$S_{\text{DCSF}}(\tau, \nu) = \sum_{[k_{\text{RS}}, l_{\text{RS}}] \in \mathcal{L}_{\text{RS}}} H_{k_{\text{RS}}, l_{\text{RS}}} e^{-j2\pi\nu l_{\text{RS}} T_o} e^{j2\pi k_{\text{RS}} \Delta f \tau} \quad (3)$$

where  $\mathcal{L}_{\text{RS}} = [k_{\text{RS}}, l_{\text{RS}}]$  is the set of distinct RS locations in the time-frequency grid with  $0 \leq k_{\text{RS}} \leq N_{\text{sc}} - 1$  and  $0 \leq l_{\text{RS}} \leq N_{\text{symb}} - 1$ .

This can be interpreted as the Monte Carlo integration of the continuous SF, which is a valid approximation. Monte Carlo integration uses random sampling of a function to numerically compute an estimate of its integral, [56]. If the RSs were completely randomly placed, we could expect the directly computed SF to converge with the full grid SF. Since the NR standard imposes some structure, e.g., due to the RSs taking specific positions, small deviations from this theory can be expected. While a theoretical investigations of these deviations on the statistical convergence is beyond the scope of this paper, we provide intuitions for the deviations in the following discussions (with respect to delay-Doppler ambiguities and sidelobe levels).

#### F. Performance Evaluation

Sec. III-D has discussed that the characteristics of CSI-RS and DM-RS make them suitable for sensing. We will analyze their impact on the SF computation and on the resulting MPC parameter estimation. This section evaluates the performance of the resulting parameter extraction in one-MPC signal models, see Sec. IV for multiple-MPC scenarios.

1) *Signal model*: In the presented examples, we use the following signal model. For 5G-NR signal characteristics,  $N_{\text{sc}} = 420$ ,  $N_{\text{symb}} = 1400$  (100 slots), subcarrier spacing = 15 kHz,  $T_o = 71.429 \mu\text{s}$ . We then consider the following RS configurations: periodic CSI-RS with frequency density = 3, repetition interval = 4 slots, random DM-RS = 25 slots out of the 100 available slots have PDSCH data allocated for the UE, DM-RS mapping type A, configuration type 1, and no precoding. We further consider the following category distributions of the PDSCH randomly allocated to a slot: i) uniform throughout the sensing interval [*uniformly random* (UR) DM-RS], specifically 25 slots uniformly random among the 100 slots; ii) distribution is dense in some parts of the sensing interval and sparse in others [*dense-sparse* (DS) DM-RS], specifically 11 slots in each of slots 1–12 and slots 89–100, and 3 slots among slots 13–88. In the CSI-RS–DM-RS combination, our simulations assume that no PDSCH is allocated in the CSI-RS slots; this is the case during the early deployments of 5G although the PDSCH may have been allocated recently in the CSI-RS slots. Accordingly, we first present the effects of RS allocation in the time domain on the Doppler identification ability and assume that the PDSCH allocated to a slot extends throughout the active BWP. Later, we analyze the frequency domain allocation of the PDSCH using the following models:

- The 2D pattern formed by the Kronecker product of the two random 1-D patterns (one in time and one in frequency). For every transmission slot, we select the same 8 RBs among the 35 RBs drawn from the uniform distribution.
- For every slot chosen to have transmission according to a random 1-D pattern in time, the set of RBs allocated in the frequency domain is selected from a different random realization of the distribution. For every transmission slot,



we select 8 RBs among the 35 RBs drawn each time from the uniform distribution.

We assume the following environment: a static BS at [0 0 0] m and a static UE at [585.9375 0 0] m. The received signal is one-MPC model,  $N_{MPC} = 1$ ,  $\nu_1 = 0$ , stemming from a static scatterer at [681.1756 0 0] m. Note that the LoS signal has been ignored and the RX is synchronized to the LoS signal. For easier representation, these numbers were chosen to provide an integer number of delay samples. The true distance between the UE and the MPC is 95.2381 m. However, the received signal has traveled an excess distance of 2 times the true distance when compared to the LoS. The excess delay encountered by the signal is 634.92 ns assuming the speed of light is  $3 \times 10^8$  m/s. The delay resolution in the SF is  $(1/BW) s = (1/(420 \times 15000)) s$ . This leads to the true delay of 4 samples for the considered MPC.

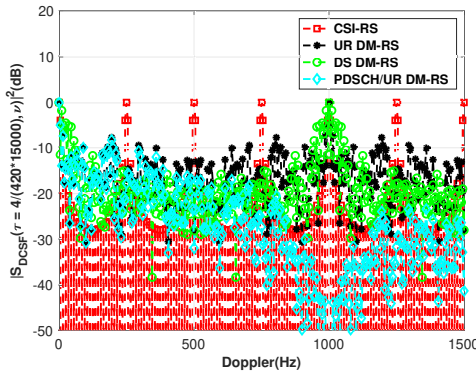


Fig. (2) Impact of RSs periodicity on Doppler detectability. Doppler = [0:5:1500] Hz. The results are symmetric to  $\nu = 0$ .

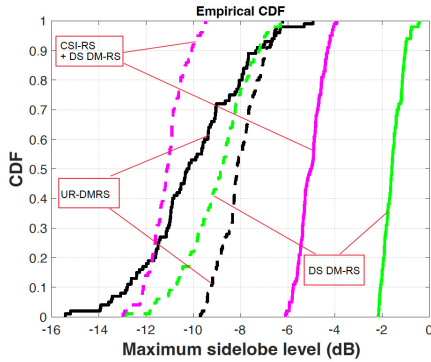


Fig. (3) Impact of RSs randomness on the maximum sidelobe level of the SF. All parameters except for the Doppler search are used as in Fig. 2. A total 100 RSs realizations, Doppler = [0:1:1500] Hz, solid lines = 10–50 Hz, dashed lines = 51–500 Hz.

2) *Performance metric 1 - Doppler and delay ambiguity*: If the time-frequency plane was completely filled by RSs, then the maximum delay and Doppler that we can estimate without ambiguity is given by the frequency and time sampling rates, respectively. This limitation arises from sampling continuous time-frequency signals, according to the Nyquist theorem. However, if the signals are sparser in time and frequency, their effective sampling rates reduce, thus reducing the maximum unambiguous delay and Doppler. The spacing between the RSs and the particular periodicity of the patterns in a configuration determines the range of unambiguous Doppler and delay values. This range must cover the delay and Doppler values

encountered in vehicular environments. In the following, we analyze the SF of different RSs computed at the true delay,  $|S_{DCSF}(\tau = 4/(420 \times 15000) s, \nu)|^2$ ; we ignore the effects of noise since the signal structure characterizes this metric.

**CSI-RS** - This signal is periodic, and thus shows Doppler aliasing with the repetition frequency equal to the inverse of periodicity. Fig. 2 shows an example of such, with time periodicity of 4 ms, which leads to Doppler aliasing with integer multiples of 250 Hz; this is smaller than the Doppler from fast-moving targets.

**DM-RS** - Randomly placed RSs break the periodicity of the samples; thus, the resulting SFs are without periodic repetitions in the Doppler domain, see UR DM-RS in Fig. 2. However, the DM-RSs are allocated only *semi-randomly*: although the PDSCH allocation to a slot may be random, the DM-RS position *within* the slot is often fixed.<sup>7</sup> Thus, for a slot duration of 1 ms corresponding to 15 kHz subcarrier spacing, DM-RSs result in Doppler ambiguities every 1 kHz, see Fig. 2. The non-aliasing region is larger i) if the BS can configure the location of the DM-RSs to be at different locations within the slot or if it is further randomized through mini-slots, and/or ii) if multiple DM-RSs are located within one slot, and/or if higher subcarrier spacing (and thus shorter slot durations) are used.

**PDSCH symbols with DM-RS** - The non-aliasing region of 1 kHz can be further extended by using the successfully decoded PDSCH data symbols allocated to the UE as pseudo-RSs. This occurs because although DM-RSs always occur in conjunction with PDSCH data, the latter can be on contiguous OFDM symbols. Fig. 2 illustrates the case where the ambiguity of 1 kHz is absent. While it has been shown that the probability distribution of payload data impacts the sensing performance [57], [58], however, with the simplification in the formulation mentioned in Sec. II, we get an *ambiguity function* (AF) which is independent of the probability distribution of the bits.

Note, however, that we will not consider the PDSCH symbols in the subsequent simulations to limit the number of signal combinations in our simulation results.

**CSI-RS with DM-RS** - The CSI-RS–DM-RS combination shows an unambiguous Doppler limit of 1 kHz, i.e., the smallest common multiple of the ambiguities of the two RSs.

**Extension to frequency domain** - The impact of RS periodicity in the frequency domain can be similarly analyzed. For example, in CSI-RSs with frequency periodicity of 4 REs = 60 kHz, there are delay ambiguities at offsets of integer multiples of 5 km.<sup>8</sup> Similar to the time domain, the randomness of DM-RS extends the delay ambiguity to 10 km (determined by the DM-RS frequency density, which is set by the DM-RS configuration type). This can be seen in Fig. 4. However, the maximum excess delay (the delay difference between the LoS and the MPC from the farthest “significant” reflector [7, Ch 6]) is limited by the length of the cyclic prefix. Since the 5G-NR cyclic prefix is of length 4.69  $\mu s$ , the maximum range the system can sustain without *intersymbol*

<sup>7</sup>The BS may choose from a set of possible configurations in each slot but can—and often will—choose the same one.

<sup>8</sup>For easier physical interpretability, delay is expressed here as distance.

interference (ISI) is 1407 m. We henceforth do not focus on the maximum delay since most MPCs in the vehicular systems occur with less than 500 m excess “delay”.

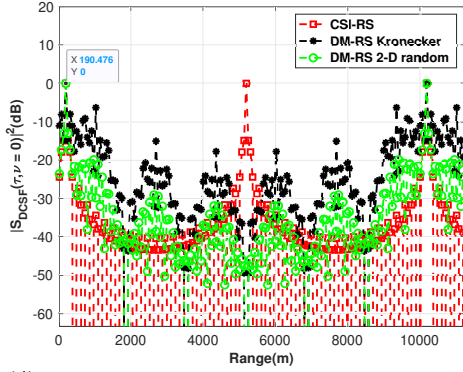


Fig. (4) Impact of RSs frequency domain periodicity on delay detectability. Range = [11.9048:59.5238:12488.095] m.

3) *Performance metric 2 - Sidelobe levels:* The sidelobes in the ambiguity function of the sensing sequence, or equivalently the SF of the single-MPC case, impact the sensing problem. The ideal SF corresponding to a target is a delta function at the specific delay-Doppler values. However, due to the finite resolution in time-frequency and finite BW and observation intervals, we get a function that has a main lobe and sidelobes. i) In the case of single MPC parameter extraction that interprets each SF peak as an MPC, sidelobes create spurious peaks that are misinterpreted as MPCs, thus leading to *false alarms* (FAs) ii) In multiple target scenarios, the sidelobes from strong reflections emerging from, e.g., clutter scatterers, swamp the weaker reflections arising from target scatterers, thereby leading to *missed detections* (MD). These effects are especially pronounced if the SF is analyzed directly through the peaks in (3), and motivates the use of SIC, see Sec. IV. In SIC and in even more advanced and complex estimators like iterative maximum-likelihood estimators, sidelobes can degrade the *receiver-operating characteristic* (ROC) curve, either inherently or due to unavoidable practical effects, e.g., imperfect calibration. Thus, maintaining low sidelobe levels in the SF is important. To evaluate the sidelobe levels, we plot the empirical *cumulative distribution function* (CDF) (over the ensemble of random DM-RS locations) of the maximum sidelobe levels in the SF that has been evaluated at the true delay  $|S_{DCSF}(\tau = 4/(420 * 15000), \nu)|^2$ , see Fig. 3. In Fig. 3, the sidelobes of the Doppler ranges we consider are 10 – 50 Hz and 50 – 500 Hz.<sup>9</sup> We then evaluate the sidelobe levels associated with the following choice of RS distributions.

**CSI-RS** - The benefit of using periodic RSs is that they lead to the sinc-shaped SF pattern, of which the sidelobe amplitudes decay inversely with the distance from the main peak. The main lobe width is given by  $2/N_{\text{symp}}T_o$ .

**DM-RS** - The insight of the magnitude of the maximum sidelobe level decreasing linearly with the number of nonzero samples has been studied extensively in the field of randomly spaced antenna arrays [59], [60]. The precise pattern of sidelobes depends on how the sampling locations

are distributed. Fig. 3 compares the UR and the DS CDFs at the range 10–50 Hz. The results show that the long gaps in the samples (DS DM-RS) lead to a slower drop of the correlation pattern from its peak, as compared to that from more evenly spaced arrangements. From the 50 – 500 Hz CDFs in Fig. 3, the UR and the DS DM-RS have fairly similar levels (much higher than uniform sampling). Critically, the sidelobes also do not die as the frequency difference from the peak increases, unlike those in the sinc pattern of CSI-RS.

**CSI-RS with DM-RS** - This combination is beneficial when there are significant gaps in the PDSCH allocation to the UE. Fig. 3 shows this as the sidelobe levels decrease for the combination as compared to the DS DM-RS allocation. The periodic CSI-RS provides a better sampling spread across time, thus improving the sidelobe pattern.

**Extension to frequency domain** - The impact of RSs randomness in the frequency domain can be similarly analyzed. Sampling uniformly across frequencies reduces the sidelobe levels in delay, whereas large gaps in the frequency domain lead to higher levels. It can be seen, from Fig. 4, that the 2D pattern formed by the Kronecker product has higher sidelobes than 2D random pattern. Similar to the time domain, using periodic CSI-RS can alleviate this issue.

4) *Performance metric 3 - Estimation accuracy in noise:* The noise in the receiver has effects on both the MPC detection and parameter estimation. The more the noise, the less the probability of detection for a given FA probability. Similarly, the variance of the parameter estimates are higher. The impact of the RS distribution on the MPC parameter estimation can be assessed by comparing the estimation variance to the *Cramer-Rao lower bound* (CRLB), which is a standard performance metric for analyzing unbiased estimators. The delay and Doppler corresponding to the SF peak is the *maximum likelihood* (ML) estimate [61] of the MPC parameters. An estimator of such form is nonlinear and can be biased when the *signal-to-noise ratio* (SNR) is below a particular threshold. However, in high SNR conditions, the estimator is unbiased, and its performance approaches the CRLB. Further, the SIC algorithm, discussed in Sec. IV, approximates an ML estimator for delay and Doppler [62].

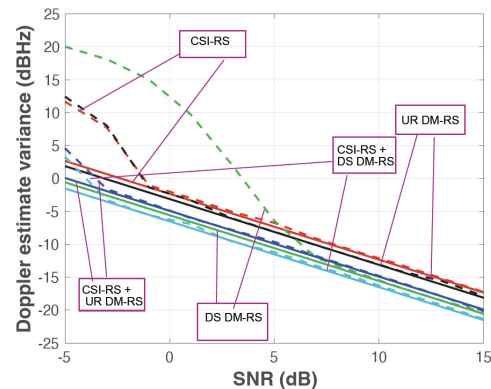


Fig. (5) Theoretical bounds vs Doppler variance.  $N_{sc} = 1$ , Doppler = [-125:0.01:125] Hz. All the other parameters are used as in Fig. 2. Solid lines = CRLB, dashed lines = Doppler variance.

<sup>9</sup>The considered sensing interval is 100 ms, which corresponds to a Fourier resolution of 10 Hz.

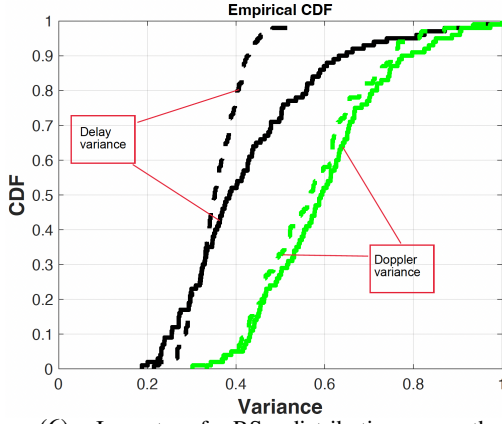


Fig. (6) Impact of RS distribution on the delay and Doppler variance. SNR=6dB Doppler [-100:5:100] Hz, delay = [0:0.5:6]/(420\*15000) s. The delay variance is normalized by  $1.15 \times 10^{-16} \text{ s}^2$ , Doppler variance is normalized by  $0.29 \text{ Hz}^2$ . Solid lines = Kronecker, dashed lines = 2-D random. All other parameters are used as in Fig. 2.

For simplicity, we consider randomly distributed RSs in the time domain (now all assumed to be in one subcarrier). This is equivalent to the Doppler frequency ML estimation of a complex exponential signal, which uses  $R_s$  nonuniform samples with sampling indices given by  $l_{RS}$ . The corresponding CRLB for the ML estimate  $\tilde{\nu}$  is [63]:

$$\text{var}(\tilde{\nu}) \geq \frac{1}{2\text{SNR}} \frac{1}{R_s \sigma_{l_{RS}}^2} \frac{1}{(2\pi T_o)^2} \quad (4)$$

where  $\sigma_{l_{RS}}^2$  represents the variance of the nonuniform sampling indices. If all the subcarriers in the allocated time symbol are used for transmission, the SNR can be improved by a factor of  $N_{sc}$ . In the special case in which all sampling indices in time range from 0 to  $(N_{\text{symb}} - 1)$ , this variance becomes  $(N_{\text{symb}}^2 - 1)N_{\text{symb}}/12$ , thereby recovering the result in [61], [64].

In Fig. 5, we consider an example for Doppler estimation using one subcarrier. We compute the SF at the true delay  $|S_{\text{DCSF}}(\tau = 4/(420 \times 15000) \text{ s}, \nu)|^2$  using one realization of the RS locations in the time domain, generated according to the specified distributions. The Doppler estimate is formed by extracting the frequency corresponding to the SF peak. It is made sure that the resolution of the search grid for extracting the frequency is sufficient so as to not encounter quantization issues. We further compute the Doppler estimate variance across 1000 runs by varying the noise realizations generated from a complex Gaussian distribution, where the noise variance is set according to the specified SNRs. Fig. 5 shows that the CSI-RS and UR DM-RS present a similar behavior in terms of the MPC parameter estimation accuracy at high SNR. The SNR threshold below which the Doppler estimation variance deviates from the CRLB is  $\approx 2 \text{ dB}$  higher in UR than in CSI-RS. Fig. 5 further suggests that the DS DM-RS has a smaller Doppler variance than the CSI-RS or the UR DM-RS at high SNR. However, the threshold SNR below, which the Doppler estimation variance deviates from the CRLB, is  $\approx 5 \text{ dB}$  higher for DS than for the UR. This can be interpreted as an effect of their respective sidelobe patterns, see Fig. 3. The sidelobes of the correlation die down more slowly in the DS than in the UR, thus leading to a higher Doppler variance in conditions of low SNR.

Summarizing, although specific extreme nonuniform sampling configurations with long gaps exhibit better Doppler variance at high SNR, they may not be as robust to noise as UR. Also, the CSI-RS–DS DM-RS combination decreases the estimation variance since there are more available samples and since the SNR threshold that deviates from CRLB is lower due to better sidelobe pattern.

This analysis can be extended to the frequency domain. As such, we generate the empirical CDF of the delay and Doppler variance formed by varying realizations of the 2-D pattern of the RS allocation. In Fig. 6, we consider the PDSCH allocation with UR in the time domain; in each used slot, the RB allocation in the frequency domain is according to the setups described in Sec. III-F1. We compute the SF using a random realization of the 2-D RS pattern. We then compute the delay and Doppler estimates by extracting the delay and frequency corresponding to the SF peak. We further double the delay and Doppler resolution in every iteration for 10 iterations to get an accurate estimate, see Sec. IV-C. Taking 100 different noise realizations, we compute the delay and Doppler estimate variances. To understand the variability of the variances with the 2-D RS pattern, we generate 100 realizations of the pattern and plot the empirical CDF of these variances, see Fig. 6. Due to its improved delay sidelobe patterns, the delay performance of the 2-D random configuration is better than that in the Kronecker 2-D random configuration. Meanwhile, the Doppler performance of both structures is almost the same since its performance is independent of the RS frequency distribution in each slot.

5) *Choice of RS for sensing*: Based on the above metrics for evaluation, the CSI-RS alone will be insufficient for sensing due to its limited unambiguous Doppler range, see Fig. 2. Although DM-RS has wide unambiguous Doppler range, it can suffer from poor sidelobe pattern that further leads to poor MPC parameter estimation performance, see Figs. 3 and 5. Combining CSI-RS and DM-RS provides the best solution as it: i) maintains the unambiguous range of DM-RS, ii) uses the CSI-RS periodicity to improve the sidelobe pattern of DM-RS, and iii) uses the available samples fully, thus increasing the sensing SNR. The issue in which the sidelobes do not die with frequency difference from the peak still persists in this combination. However, this will be solved in the next section through SIC. Precoding the DM-RS can introduce additional problems, which will be discussed in Sec. V.

#### IV. IDENTIFYING SIGNAL ECHOES

##### A. Motivation

Sec. III has shown that random RSs lead to cross-correlation sidelobe levels that affect the performance in multi-target scenarios. Sidelobe levels are typically no more than 10 – 15 dB below the main peak, thus leading to excessive performance loss in Fourier (peak detection) analysis. This is because the sidelobes are identified as additional targets and because some target echoes get buried in the sidelobes of other stronger scatterers.

##### B. SIC

The following are the steps in conducting a multipath detection via SIC, also known as the CLEAN algorithm:



- Create a hypothesis grid in the delay-Doppler plane. Compute the SF at each point in the hypothesis grid and then find the delay-Doppler with the maximum power. This is the delay-Doppler estimate of the strongest target.
- Reconstruct the contribution of this strongest target to the received signal using the amplitude, delay, and Doppler estimates of the thus-found peak.
- Subtract the reconstructed signal from the original signal. Repeat these steps until the difference between the power of the peak in the first iteration and the power of the peak in the current iteration is above a certain threshold or until the number of extractions reaches the set limit (set to 30 in our examples).

The successive peaks found in the algorithm steps correspond to the targets with their respective delay-Doppler values. This can be further refined for iterative improvements (SAGE, [65]) and gradient search (RiMax, [66]). However, if the number of significant targets impacting each other's contribution is low, then the improvements through the iterative approaches such as SAGE would be low as well. Since this condition is fulfilled in the following simulations, the evaluations are based on the “standard” SIC [7, Ch. 9]. Further, there are super-resolution methods like [67] that have been shown to extract closely spaced target echoes efficiently. However, these methods cannot be directly used here due to the presence of nonuniformly distributed RSs.

The choice of grid points requires various trade-offs. A denser grid leads to a more accurate parameter extraction. This is not only important by itself, but also because misestimating the target coordinates and the resulting subtraction of the SF contribution centered on a slightly offset location can lead to an imperfect subtraction that leaves a residue. The algorithm interprets this residue as an additional target, also called “ghost target”. Conversely, a fine grid increases the computational effort. Accordingly, a heuristic solution to this problem is an iterative grid refinement: we obtain initial estimates from a coarse grid with a delay spacing of 0.5 samples and a Doppler spacing of 5 Hz. The search range in the next iteration is limited to the delay-Doppler vicinity of the extracted targets of the current iteration while the resolution of delay and Doppler spacing is increased by a factor of 2. This process is repeated 5 times. Although this approach does not guarantee global optimality, it still provides a good approximation.

### C. Simulation Results

We use the CSI-RS-UR DM-RS combination to perform sensing in this setup. We assume that there is randomness only in the time domain allocation of the PDSCH, while the allocation in the frequency domain is throughout the active BWP, see Fig. 2. We use an “Urban Street Canyon” model for scatterers to evaluate the performance. This model is defined by the static BS at [0 0 0] m and static UE at [976.5625 0 0] m located at the street center. On either side of the 24-m-wide street, four buildings, spaced 20 m apart from each other, are present. The street has four lanes, 4 m apart with two lanes each going in either direction. In each lane, cars move with velocities uniformly distributed between 0 and

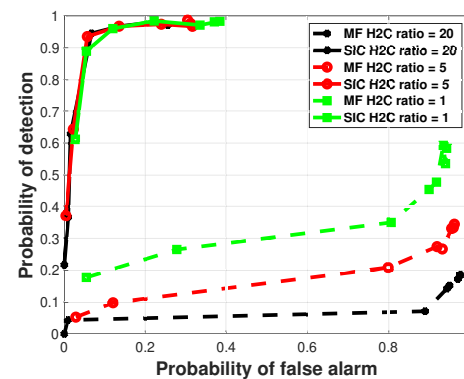


Fig. (7) Comparison of ROC between SIC and Fourier processing. Delay = [0:0.5:6]/(420\*15000) s, Doppler = [-500:5:500] Hz, All other parameters are used as in Fig. 2

25 m/s. Their direction depends on which side of the street center the vehicles are at. The cars are distributed along the lane according to a one-dimensional homogeneous Poisson point process, with an average of two cars per 50 m in a lane. Further, the radar cross-section of the houses varies, i.e., 100 m<sup>2</sup>, 25 m<sup>2</sup>, 5 m<sup>2</sup>, while that of the cars is kept at 5 m<sup>2</sup>.<sup>10</sup>

As a baseline to compare the SIC against, we use conventional *matched filter* (MF) techniques to extract the MPC parameters. Hence, we create a hypothesis grid in the delay-Doppler plane and compute the SF as described in Sec IV-B. We extract the maxima sequentially in the SF until the power difference between the global maximum and the maximum under consideration is above a certain threshold. The cross-correlation sidelobes of the stronger maxima extending throughout the delay-Doppler plane makes it hard to detect weaker local maxima in the SF. The ideal cross-correlation follows the sinc-shaped pattern; thus, we reject those maxima that are less than 1 dB above the level expected by the sum of the cross-correlations of the previously extracted maxima evaluated at the delay/Doppler of the candidate maximum. We also limit the number of selected maxima, here 75, to simplify the algorithm. We use the same iterative grid refinement, as described in Sec IV-B, to ease the computation.

There are mainly two types of *clutter suppression* (CS) in the literature (i) Pre-extraction CS and (ii) Post-extraction CS. In the pre-extraction algorithms, the clutter is subtracted from the signal, and then the target parameters are extracted. These methods are popular in radar literature, e.g., DPCA, [68], STAP, [69], etc. In contrast, the post-extraction algorithms extract all the MPCs and then filter the clutter components, [70]. This is usually done based on the relationship between the extracted parameters. While most of our discussion can be combined with either of those approaches, our examples based on SIC take the second approach. Since the BS and UE are both assumed to be static, the expected Doppler of

<sup>10</sup>Note that the target cars located on the street *between* the BS and the UE are not considered here because the induced Doppler shift is almost zero, thus making them almost indistinguishable from static echoes in the Doppler domain. This problem and its possible solutions will be explored in future work.

the clutter components is 0. This allows to identify the echoes with Doppler components below a certain threshold as clutter.

Once both the algorithm, i.e., SIC and MF, extract the MPC parameters, since both the BS and UE are static, we identify all the scatterers with a Doppler shift of  $>25$  Hz as the intended targets. In the case of moving UE, elimination of static objects requires more complicated processing, [69], and is outside the scope of the current paper. We further define the criteria for FAs and MDs. Note that the LoS signal has been ignored and the RX is synchronized to the LoS signal. If the extracted target is within its associated detection region, defined as  $\Delta\tau = 0.25/(420 \times 15000)$  s delay and  $\Delta\nu = 2.5$  Hz Doppler of the true target, then it is classified as a detection. An FA is defined as the ratio of the number of extracted targets that do not have any true targets in its associated detection region to the total number of extracted targets. Similarly, MD is defined as the ratio of the true targets that do not have any extracted targets of which the decision region overlaps them, to the number of true targets. In a given extraction threshold, we compute the *probability of false alarms* (PFA) and *probability of detection* (PD) by averaging FA and  $1 - \text{MD}$  for 100 random scenario realizations, respectively, generated from the “Urban Street Canyon” model. We then plot the PFA against the PD by varying the extraction threshold called the ROC curve, which is the standard performance metric for detection problems.

Fig. 7 shows that the SIC performs better than the MF techniques due to the reasons discussed in Sec. IV-A. This advantage is most pronounced when the clutter echoes are much stronger than the target signals (thus burying the target signals in the sidelobes). The SIC removes the MPCs in decreasing order of their strength. The stronger components are initially estimated and removed, which allows the weaker components to be estimated. However, we have not yet identified the clutter echoes. For the post-extraction CS, echoes with Doppler below a certain threshold are considered to be clutter. Since these components are typically higher power than the targets, these are estimated and removed initially in the SIC operation. The decreasing performance of the MF target extraction as the clutter radar cross section increases confirms this finding.

We also evaluate the SIC results across different realizations of DM-RS configurations. We use the same channel model as in Fig. 7, with the radar cross section of the houses set to 100. For a given DM-RS and scenario realization, we set a threshold of 35 dB for the SIC extraction and then compute the delay and Doppler *mean square error* (MSE). The MSE for parameter extraction is defined as the mean of the squared error between the true target parameter and the SIC extracted target parameter over the number of detected targets. The MSE is further averaged over the 100 random scenario realizations of the channel model.

Then, we generate 50 realizations from the distribution that defines the RS placements in the time domain and plot the CDF of the delay and Doppler MSE. Fig. 6 shows that the Doppler variance of the CSI-RS combined with the DS DM-RS is smaller than that with UR DM-RS. This is because the CSI-RS–DS DM-RS combination has lower variance than the CSI-RS–UR DM-RS combination, see Fig. 5. The PDSCH

distribution in the time domain should not affect the delay variance. However, a difference can be seen in Fig. 8 which may be due to i) the different number of slots selected in these cases (the constraint that the PDSCH cannot be allocated to the CSI-RS slots causes this difference), and ii) the different number of detections in these cases (UR has slightly more detections than the DS due to lower sidelobes).

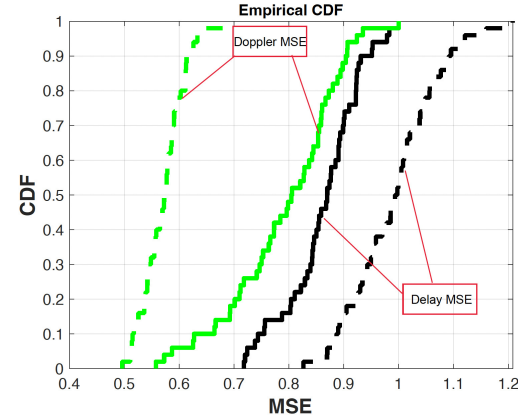


Fig. (8) SIC results across RS configurations. Delay MSE normalized with  $1.52 \times 10^{-16} \text{s}^2$ , Doppler MSE normalized with  $0.9 \text{ Hz}^2$ . Solid lines = CSI-RS + UR DM-RS, Dashed lines = CSI-RS + DS DM-RS.

## V. ACCOUNTING FOR TX PRECODER EFFECTS

### A. Beamforming and Precoding

The multiple antennas in an NR BS usually send out weighted replicas of the signal intended for a particular user. The weighting is done in two steps: beamforming and precoding. Typically, beamforming is based on the second-order statistics of CSI (angular power spectra), independent of frequency, and serves to point a beam in the direction of an RX to enhance SNR; this is especially prevalent in *frequency range 2* (FR2). In contrast, precoding is based on instantaneous CSI. It can differ in different subcarriers and is often used to minimize, e.g., zero-force interference in *multiuser multiple-input multiple-output* (MU-MIMO) transmission.<sup>11</sup> In NR, the subcarriers are grouped into *physical resource block groups* (PRG), and the precoding is constant over one PRG. Precoder settings are based either on channel reciprocity or on the feedback that the UE sends to the BS in the CSI report. This report contains the *precoding matrix indicator* (PMI) as the index of the precoder codebook entry that should be used.

Even though, in this work, we consider a single-stream system, we analyze the impact of *multiple-input multiple-output* (MIMO) precoding. The precoding alters the beam pattern of the transmit waveform, thus altering the amplitude and phase of MPC paths. This precludes us from combining the signals arising from different precoding matrices. Therefore, the time-frequency resources in which the beamformer and precoder settings remain constant are critical to the sensing performance and are also controlled by the BS. Beamforming may not be applied in FR1, and even if it is, we assume that the beamforming pattern does not

<sup>11</sup>This distinction between beamforming and precoding is based on the typical usage in current NR systems but is not defined as such in the standard.

change during the sensing interval. Precoding is often applied in FR1 systems. In the frequency domain, the BS precoding using “wideband” setting is based on the feedback from the UE for the whole BWP; thus, the same precoding is applied to all the allocated resources within the BWP. Alternatively, the BWP can be divided into several PRGs, each of which is precoded using a particular setting based on the feedback specifically intended for each of them. In the time domain, new precoder settings are usually based on a request from the BS. This then triggers the CSI, i.e., a PMI, to be computed in the UE at the next available CSI-RS, and for the UE to transmit this information in a CSI report. The design of beamformers at the BS that optimize sensing performance under the constraint of communications performance has been studied in ISAC systems, e.g., [71]. If the BS decides to beamform towards the user, the interesting targets that are not in this direction cannot be sensed at the UE and might require a modification in the BS beamformer settings. This information can be sent to the BS in the CSI report. Upon receiving this report, the BS can alter the precoding matrix it uses. However, the BS may also ignore the suggestion from the UE for a specific precoding matrix and use its discretion instead; in this case, the UE would not know when and to what values the precoding matrix would change.

### B. Motivation

The assumption that RSs are not precoded may not always be fulfilled in FR1. Sec. III-D has discussed that the BS may precode certain RSs depending on the system requirements. In particular, DM-RSs are usually precoded, thus preventing them from being combined with the not-precoded CSI-RSs to enhance sensing performance. Also, the BS may choose different precoding vectors for the DM-RSs in different PRGs (based on the feedback from the UE or arbitrarily decided by the BS). Moreover, the precoder settings in each PRG might change as fast as every 2–4 subframes. Since this assignment may be unknown to the UE, computing the SF across DM-RSs with different precoders and extracting targets using SIC can result in numerous FAs.

### C. Methods

One solution then is to identify the DM-RSs that use the same precoder settings. To achieve this, we first identify the DM-RSs belonging to a *contiguous* set of PRGs in the time-frequency plane that use the same precoder settings (henceforth, called *sub-bands*). To determine the sub-band boundaries, we must analyze the discontinuities of the estimated channel phase between the neighboring OFDM symbols and subcarriers. Since the target parameters, i.e., delay, Doppler, and power, are constant within the observation interval and bandwidth, any discontinuity seen in the composite channel estimate phase of the DM-RSs can be interpreted as due to a change in the precoder settings. Note that the 3GPP standard definition prescribes that the precoder must be identical within a PRG, and thus only phase discontinuities at the boundary between PRGs need to be checked.

However, sub-band-wise processing leads to poorer results since the SF computed within a sub-band only leads to low

resolution in the delay-Doppler domain due to the possibly low BW and observation time. This problem can be alleviated if the BS precodes multiple disjoint sub-bands using the same precoder settings. This would allow us to exploit a larger BW and observation interval, thus improving resolution and combating noise.

Once the sub-band boundaries are obtained, we employ the following algorithm to identify the similarities in the target parameters across sub-bands and determine whether or not they use the same precoder settings. The following steps are shown as pseudo-code in Algorithm 1.

---

#### Algorithm 1 Sub-band grouping algorithm

---

- 1: Using SIC, extract the strong scatterers and remove the ghost paths in each sub-band.
  - 2: In each of the strong scatterer in every sub-band, find the scatterer closest (in delay-Doppler domain) in all other sub-bands.
  - 3: Check if the closest scatterer is “similar” to the considered scatterer.
  - 4: Compute the *precoder similarity index* (PSI) using the algorithm explained in 2) for each sub-band pair based on the similarity votes of scatterers.
  - 5: If the PSI of a given sub-band pair under hypothesis  $\geq 0.5$ , decide that the two sub-bands would use the same precoder.
  - 6: If the PSI of some of the sub-band pair produces “conflicts”, then do not group the sub-bands.
- 

- 1) The SIC algorithm extracts the delay-Doppler-power estimates of targets (after Doppler filtering to remove clutter) in each sub-band. We consider the *strong targets*, i.e., with power within T dB,  $T = 20$  in our examples, of the power of the strongest target in each sub-band. We remove the ghost targets based on proximity (to the delay-Doppler domain) criterion, which is  $\Delta\tau = 0.25/(420 * 15000)$  s and  $\Delta\nu = 2.5$  Hz in our examples, respectively, i.e., additional paths within this region around an already extracted target are regarded as ghost targets. We do this because ghost paths can distort the PSI computation.
- 2) For each identified strong target in a sub-band, we find the closest (sum of the normalized delay-Doppler differences) target in every other sub-band. The normalizations for delay difference and Doppler difference are 1/100 s and 1 Hz, respectively. We declare that the two are “similar” if they satisfy the joint (sum of the normalized delay-Doppler-power differences) threshold defined as  $T_1$ , which is set here as 75. The normalization for power difference is (1/10) dBW. We then compute a metric  $PSI_{i,j}$  that gives the fraction of strong targets in the sub-band  $i$  that has a corresponding “similar” strong target in sub-band  $j$  according to the following algorithm:

```

1: for  $i \leftarrow 1$  to  $N_{sb}$  do
2:   for  $j \leftarrow 1$  to  $N_{sb}$  :  $j \neq i$  do  $PSI_{i,j} = 0$ 
3:     for  $k \leftarrow 1$  to  $M_i$  do
       Find the closest target to  $str_i(k)$  in the set  $str_j$ :
        $minind = \arg \min_{str_j(m)} 100 * |\hat{\tau}_k - \hat{\tau}_{j_m}| + |\hat{\nu}_k - \hat{\nu}_{j_m}|$ 

```

```

 $minval = \min_{str_j(m)} 100 * |\hat{\tau}_k - \hat{\tau}_{j_m}| + |\hat{\nu}_k - \hat{\nu}_{j_m}|$ 
Check if the closest target meets the similarity criterion:
4:   if  $\max(minval, 25) + 10 * |\alpha_k - \alpha_{minind}| \leq$ 
 $T_1$  then
         $PSI_{i,j} = PSI_{i,j} + 1/M_i$ 
5:   end if
6:   end for
7: end for
8: end for

```

where the SIC delay-Doppler-power parameters of the extracted strong targets in each sub-band are denoted by  $str_p = \{(\hat{\tau}_1, \hat{\nu}_1, \alpha_1), \dots, (\hat{\tau}_{M_p}, \hat{\nu}_{M_p}, \alpha_{M_p})\}$ , where the power is represented in units of dBW;  $M_p$  is the number of extracted strong targets in  $p$ th sub-band;  $N_{sb}$  is the number of sub-bands.

- 3) The grouping problem can be formulated as a detection problem. We decide whether the considered sub-band pair will use the same precoder if the average PSI of the sub-band pair is  $> 0.5$ .<sup>12</sup> This is the Bayes optimal threshold assuming equal costs for MDs and FAs. We then identify “conflict” (precoder decisions of sub-bands based on PSI not consistent with each other) between the PSI metric of sub-band pairs. If it exists, then we do not combine the sub-bands; if it does not exist, then we run the SIC algorithm on the union of the identified similar sub-bands to extract the targets of interest.

#### D. Simulation Results

We simulate the sub-band grouping algorithm using a realization of UR DM-RSs, where we select 45 out of the available 100 slots in the time domain. In the frequency domain, we consider 3 PRGs containing 11 RBs, 11 RBs, 13 RBs, respectively. We assume that the precoder settings of each PRG do not change with time. The BS and UE are assumed to be placed very close to each other with the BS at  $[0 \ 0 \ 0]$  m and the UE at  $[19.53125 \ 0 \ 0]$  m. This ensures that the different targets in the street are seen by the BS over an angular range of  $\approx 20^\circ$  at the BS. We assume the same scatterer model as in Fig. 6; except that, here, we use an average of one car per 50 m in a lane. The DM-RSs are precoded using the DFT codebook. PRGs 0 and 2 are precoded using the  $0^\circ$  beam, whereas PRG 1 is precoded using the  $22.5^\circ$  beam.

We have to identify the sub-band boundaries before we can group them. Since the signal power is high, we directly identify the phase jumps in the DM-RS channel estimate in both time and frequency. In the frequency domain, the phase jumps occur only at the PRG boundary, whereas in the time domain, there are no phase jumps. We assume that the sub-band boundaries and the resulting three sub-bands in the simulations are correctly established. A total of 100 scenario realizations are generated in the evaluation of the grouping algorithm. In each run, we compute the PSI for each sub-band pair. We then plot the empirical CDF of these values in Fig. 9 and observe the number of runs where we see “conflicts” and the number of runs we detect the sub-band groups correctly. Further, we compute the PFA, PD and MSE of the

target parameters for the individual sub-bands, combining all sub-bands (“blindly”) as well as combining only sub-bands 0 and 2.

Fig. 9 shows that the PSI in sub-band pairs 0–1 and 1–2 are, on average, smaller than the PSI in sub-bands pair 0–2. The number of runs where the algorithm detected the sub-band groups correctly are 83, and the number of runs where the PSI gave conflicting results are 7.

We also demonstrate the efficacy of combining the sub-bands. The PFA and PD of the “blind” sub-band combinations are 0.21 and 0.54, respectively. The PFA and PD of the individual sub-bands 0 and 2 are close to 0.08 and 0.9, respectively. However, the MSE of delay in these sub-bands is close to  $1.45 \times 10^{-16}$  s<sup>2</sup>. The PFA and PD of the sub-band combinations 0 and 2 are 0.05 and 0.95, respectively. Further, the MSE of delay is close to  $2.4 \times 10^{-17}$  s<sup>2</sup>. Thus, combining sub-bands improves both the detection of MPCs and the accuracy of detected MPCs.

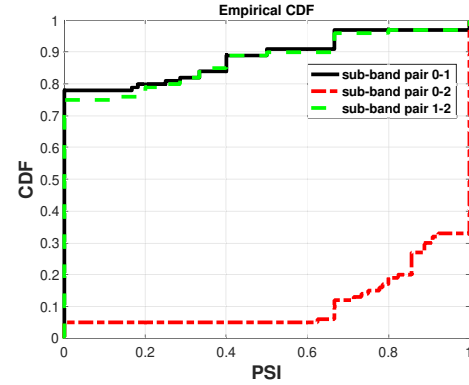


Fig. (9) CDF of the PSI in the sub-band grouping algorithm. See discussion for the settings of the precoders and the channel model.

#### E. Technical Challenges

However, this algorithm cannot be robust if the BS decides to use PRGs with few RBs, or if the BS changes the precoder settings very frequently. This results in a large number of sub-bands, each with a few time-frequency resources, thus making it difficult to identify precoder similarity between sub-bands. Combining different sub-bands might not be beneficial in this case. As such, using the results from the SIC estimates computed using individual sub-bands may be more appropriate.

#### VI. VALIDATION USING MEASURED CHANNELS

In this section, we verify the SIC algorithm within the context of *measured* propagation channels. The measurements were done with a MIMO setup and we selected a single antenna at the TX and the RX to mimic the SISO configuration assumed throughout this paper. Furthermore, these measurements were done in a V2V setup, which differs somewhat from the typical V2I setup, both in terms of frequency, and the BS height: the 5.9 GHz band in which the measurements are conducted is foreseen for V2V communications, while V2I is likely to operate in the 3.5 GHz midband, and both the nodes in the measurement are 1.5 m height, while in V2I, the BS is elevated. Thus, the details of radar cross section and signal strength might different in a V2I setup. However, our setup is still valid as a proof of the

<sup>12</sup>From each pair of sub-bands  $(i, j)$ , we get two values of PSI, and the average PSI takes the mean of the two.



principle. Furthermore, bistatic radar in V2V channels is of interest in itself.

#### A. Measurement Setup

We measured the propagation channel using a self-built real-time MIMO channel sounder, which measures the channel transfer functions between each of the 8 TX and 8 RX antennas.<sup>13</sup>

A “MIMO snapshot” measuring all these combinations lasts for  $T_0 = 640 \mu\text{s}$ . The maximum Doppler shift that can be resolved without ambiguity is  $1/2T_0, \approx 806 \text{ Hz}$ , which corresponds to a relative speed of 148 km/h with the carrier frequency of 5.9 GHz. The BW of the sounding signal is 15 MHz. The number of subcarriers is 61 ( $N_{\text{sc}} = 61$ ). TX signals are transmitted in bursts, followed by a silence period. One burst consists of 30 MIMO snapshots ( $N_{\text{syms}} = 30$ ), and the rate of bursts is 20 Hz. To illustrate the effects of RS density and distribution on sensing, the CSI-RS and UR DM-RS style assignment of time-frequency grid points are performed in post-processing, i.e., while the measurements are done on a regular grid, only the points to which the RSs are assigned are used in the algorithms to sense the surrounding targets. In the CSI-RS configuration, snapshot 1 is always scheduled to send CSI-RS in every 4th subcarrier. In the UR DM-RS configuration, the snapshots that are allocated for sensing are generated from a uniform distribution, and the probability of selecting a snapshot is given by the defined “percentage” of snapshots. Further, if a particular snapshot is selected for sensing, then we vary the number of subcarriers used for processing. It can be either using every second subcarrier for the entire BW or a specified fraction of the uniformly distributed 61 subcarriers.

#### B. Measurement Scenario

We analyzed two scenarios near the University Park Campus of the University of Southern California, Los Angeles, California, USA, in what can be classified as an urban environment. Two 360-degree cameras, one each on the TX and RX, during the measurement, recorded the environment. In our analyzed setup, both the TX and RX were static and located at an intersection. This enables simple clutter elimination through Doppler filtering, and makes it easier to interpret and verify the results.

Fig. 10 gives a sample snapshot of the scenario 1 video recorded from the RX point of view, where two nearby vehicles (targets of interest) make turns into the street where the RX is located. Fig. 12 gives a sample snapshot of the scenario 2 video recorded from the RX point of view, where a vehicle (target of interest) passes through the intersection from left to right in a direction perpendicular to the direction where the TX and RX are facing. These videos were used to obtain the ground-truth range-Doppler components of the vehicles moving nearby.<sup>14</sup> The estimated trajectories of the oncoming cars on Google Maps are presented in Figs. 11 and 13 for scenario 1 and 2, respectively.

<sup>13</sup>The detailed information about the channel sounder and the measurement campaign can be found in [72].

<sup>14</sup>The range and delay are interchangeable, where delay is range-scaled down by the speed of light.

#### C. Antenna Pair Selection, Synchronization, and Ground-Truth Range-Doppler Extraction

**Antenna pair selection** - Although we performed measurements using a MIMO channel sounder, we aim to validate a SISO setup; thus, we needed to select a suitable TX-RX antenna pair. We estimated from the geometry as to which antenna pair gave the highest LoS power and illuminated the area with targets of interest.

**Synchronization** - We computed the true distance between the TX and RX by locating them on Google Maps based on the video. At the same time, the LoS distance was computed using the channel measurements. For this purpose, we ran the SIC algorithm in each burst, and the distance corresponding to the highest-power-MPC was averaged to accurately estimate LoS distance. This distance was compared with the ground-truth distance; we used the offset (caused, e.g., by clock drift) to correct the range estimates from the SIC algorithm.

**Ground-truth range-Doppler extraction** - We estimated the positions and velocities of the target cars with the help of the videos. We assumed that the turns the cars made onto a street in scenario 1 followed a quarter-circular trajectory followed by a linear trajectory. The radius of the circle was then estimated with the help of the video and Google Maps. Meanwhile, we assumed that the cars passing through the intersection in scenario 2 followed a linear trajectory. Since the SIC has a resolution finer than the dimensions of the reflecting car surface, the target car could not be treated as a point object; instead, we considered it to be a two-point object with the two points located at the front-most and back-most points of the car, and on the side of the target car that is visible from TX and RX. This provided the limits of the range and Doppler we could expect to see. From this and from the TX and RX positions, we computed the “ground truth” range/delay and Doppler. The expected profile of the two target cars in scenario 1 is illustrated in Fig. 16. Note that the target cars were not under the control of the measurement campaign, thereby precluding direct measurement of their speed and location.



Fig. (10) Video snapshot of scenario 1.

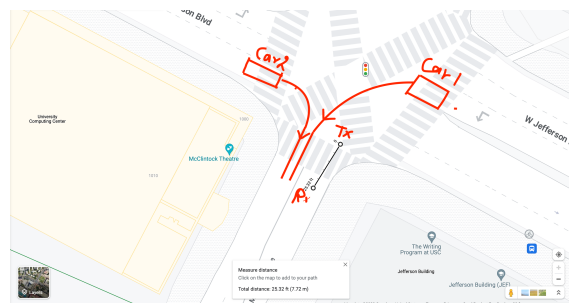


Fig. (11) Trajectory map of scenario 1.



Fig. (12) Video snapshot of scenario 2.

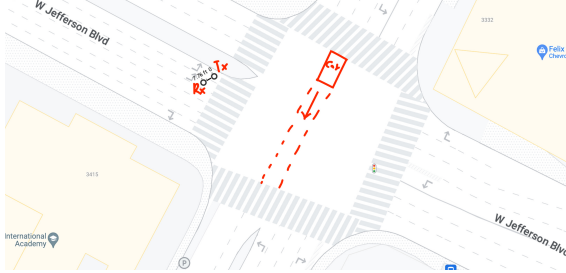


Fig. (13) Trajectory map of scenario 2.

#### D. Measurement Data Processing

We consider a realization of RS allocation drawn from a specific distribution in each burst. Using these RSs, we perform SIC to extract the MPCs in each burst. The maximum number of MPCs extracted is 20. The calibrated LoS offset amounts to a distance of 5 m, which is added to the estimated MPC range. A threshold of 25 Hz is used to classify the extracted MPCs as clutter or intended targets. Fig. 16 presents a 2-D projection of the measured range-Doppler of the extracted targets plotted across burst times, along with the ground truth range-Doppler of surrounding cars in scenario 1.

Further, a 5 m range and 25 Hz Doppler window centered on the ground-truth range-Doppler is defined. Targets with range-Doppler within this window are considered to have been correctly detected.<sup>15</sup> The window accounts for errors in position and in the velocity of target vehicles, e.g., due to the assumption of circular trajectory and the spatial extent of the target cars. The measured target echoes outside the window are considered as FAs. The FAs and detections are summed across bursts, and subsequently averaged across different realizations of the RS allocation. We vary the threshold in the SIC algorithm to get the ROC of FAs vs detections, see Figs. 14 and 15.<sup>16</sup> Further, we define the MSE metrics for range and Doppler. If the target point is considered a detection, the squared range error is computed as the minimum of the square of the range difference of the extracted target point range and the true range of the front-most and back-most points of the target. The same is done for squared Doppler error. These errors are averaged across the total number of detections to generate the MSE metrics, see Figs. 17 and 18. The figures show that the performance degrades as we reduce the time-frequency resources allocated for sensing. This is expected since i) the sidelobe levels increase due to the decrease in number of RSs and ii) the sensing SNR degrades.

<sup>15</sup>Since the targets are spatially extended, the length of the target car is added to the range window length.

<sup>16</sup>In contrast to the conventional ROC, which plots the PFA and PD, we plot here the number of FAs and detections since we cannot compute the total number of possible detections, and hence the probabilities.

The figures also show that it is not clear whether the time or the frequency randomness is more favorable in different scenarios: in scenario 1, frequency randomness does not impact sensing as much as time randomness does; in scenario 2, it is the opposite. We conjecture that this could be due to the number of targets present in the close vicinity. If they have similar ranges, then frequency randomness affects sensing. Conversely, if they have similar Doppler values, then time randomness impacts sensing performance.

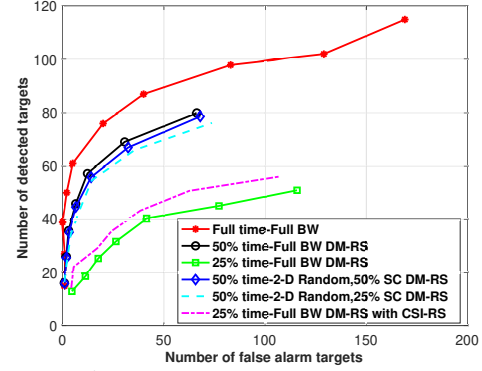


Fig. (14) Detection vs FA scenario 1.

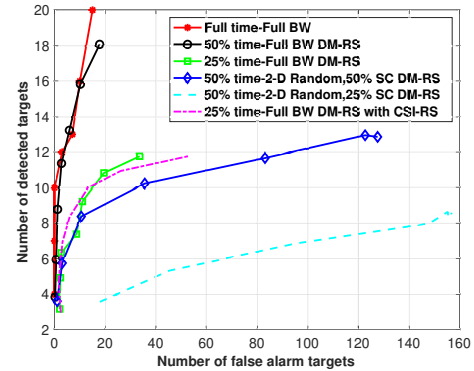


Fig. (15) Detection vs FA scenario 2.

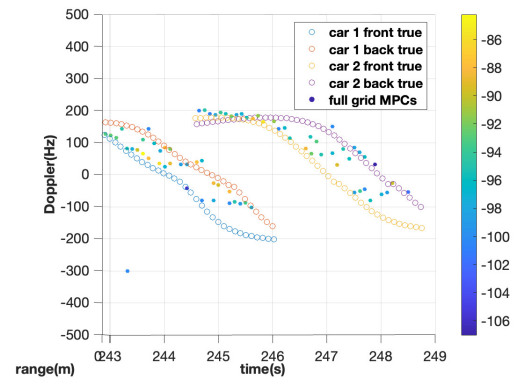


Fig. (16) 2-D projection of time-range-Doppler plot of scenario 1.

#### VII. CONCLUSIONS

In this paper, we have shown that 5G-NR signals can be used as radar signals for vehicle detection. However, since 5G-NR is a BS centric system such that the BS can arbitrarily choose to allocate a certain number of resources to the UE, the associated RSs and the precoder settings, we cannot guarantee the sensing performance. The only RSs that are certainly transmitted are the SS. However, they have a very low BW to provide any meaningful range resolution. In quasi-static

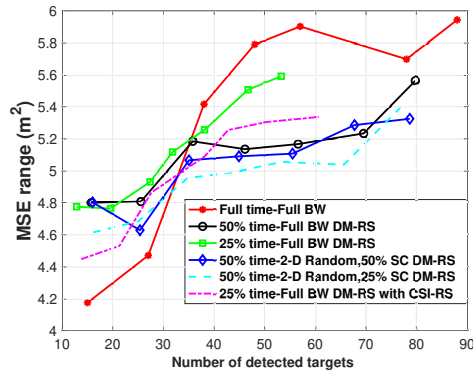


Fig. (17) Detection vs MSE range scenario 1.

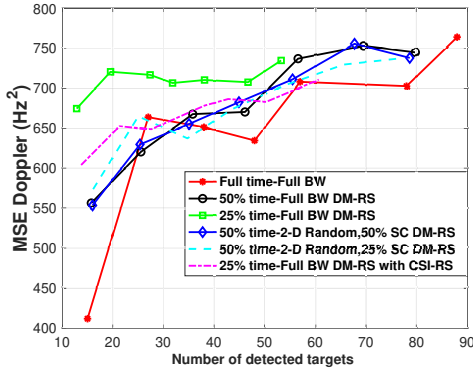


Fig. (18) Detection vs MSE Doppler scenario 1.

(like indoor) scenarios, the PRS can be helpful in positioning. Since the PRS is transmitted across the whole BW, it can provide a fine range estimation. We have also shown that a smart combination of RSs improves estimation performance. We have done this by choosing the RSs that have suitable characteristics and then combining them to enhance specific performance metrics. Such combination leads to an irregular structure of RSs that necessitates advanced processing, i.e., SIC. We have likewise presented that the precoder creates additional problems such that the RSs cannot be combined if some of them are precoded differently. Lastly, we have introduced a method for determining sub-bands with the same precoder settings.

## REFERENCES

- [1] N. K. Nataraja, S. Sharma, K. Ali, F. Bai, and A. F. Molisch, "Bistatic vehicular radar with 5G-NR signals," in *IEEE GLOBECOM*. IEEE, 2023, pp. 5605–5610.
- [2] J. Hasch, E. Topak, R. Schnabel, T. Zwick, R. Weigel, and C. Waldschmidt, "Millimeter-wave technology for automotive radar sensors in the 77 GHz frequency band," *IEEE Trans. Microw. Theory Tech.*, vol. 60, no. 3, pp. 845–860, Jan. 2012.
- [3] G. Hakobyan and B. Yang, "High-performance automotive radar: A review of signal processing algorithms and modulation schemes," *IEEE Signal Process. Mag.*, vol. 36, no. 5, pp. 32–44, Sep. 2019.
- [4] D. Solomitckii, C. B. Barneto, M. Turunen, M. Allén, Y. Koucheryavy, and M. Valkama, "Millimeter-wave automotive radar scheme with passive reflector for blind corner conditions," in *2020 14th EuCAP*, 2020, pp. 1–5.
- [5] D. Solomitckii, M. Heino, S. Buddappagari, M. A. Hein, and M. Valkama, "Radar scheme with raised reflector for NLOS vehicle detection," *IEEE T-ITS*, vol. 23, no. 7, pp. 9037–9045, Jun. 2022.
- [6] E. Dahlman, S. Parkvall, and J. Skold, *5G NR: The Next Generation Wireless Access Technology*. Cambridge, MA: Academic Press, 2020.
- [7] A. F. Molisch, *Wireless Communications: From Fundamentals to Beyond 5G*, 3rd ed. Hoboken, NJ: Wiley-IEEE Press, 2023.
- [8] M. Garcia et al., "A tutorial on 5G NR V2X communications," *IEEE Commun. Surv. Tutor.*, vol. 23, no. 3, pp. 1972–2026, Feb. 2021.

- [9] C. Sturm, T. Zwick, and W. Wiesbeck, "An OFDM system concept for joint radar and communications operations," in *IEEE VTC Spring 2009*, 2009, pp. 1–5.
- [10] M. Cherniakov, *Bistatic Radar: Emerging Technology*. Hoboken, NJ: John Wiley & Sons, 2008.
- [11] J. A. Zhang et al., "Enabling joint communication and radar sensing in mobile networks—a survey," *IEEE Commun. Surv. Tutor.*, vol. 24, no. 1, pp. 306–345, Oct. 2021.
- [12] S. Mercier, D. Roque, and S. Bidon, "Study of the target self-interference in a low-complexity OFDM-based radar receiver," *IEEE Trans. Aerosp. Electron. Syst.*, vol. 55, no. 3, pp. 1200–1212, Nov. 2018.
- [13] F. Liu et al., "Integrated sensing and communications: Towards dual-functional wireless networks for 6G and beyond," *IEEE J. Sel. Areas Commun.*, vol. 40, no. 6, pp. 1728–1767, Mar. 2022.
- [14] S. Mazahir, S. Ahmed, and M.-S. Alouini, "A survey on joint communication-radar systems," *Front. Comms. Net.*, vol. 1, p. 619483, Feb. 2021.
- [15] R. Thomä, T. Dallmann, S. Jovanoska, P. Knott, and A. Schmeink, "Joint communication and radar sensing: An overview," in *15th IEEE EuCAP*, 2021, pp. 1–5.
- [16] N. C. Luong, X. Lu, D. T. Hoang, D. Niyato, and D. I. Kim, "Radio resource management in joint radar and communication: A comprehensive survey," *IEEE Commun. Surv. Tutor.*, vol. 23, no. 2, pp. 780–814, Apr. 2021.
- [17] A. Liu et al., "A survey on fundamental limits of integrated sensing and communication," *IEEE Commun. Surv. Tutor.*, vol. 24, no. 2, pp. 994–1034, Feb. 2022.
- [18] R. S. A. R. Abdullah et al., "LTE-based passive bistatic radar system for detection of ground-moving targets," *Etri Journal*, vol. 38, no. 2, pp. 302–313, Apr. 2016.
- [19] S. Gogineni, M. Rangaswamy, B. D. Rigling, and A. Nehorai, "Cramér-rao bounds for UMTS-based passive multistatic radar," *IEEE Trans. Signal Process.*, vol. 62, no. 1, pp. 95–106, Oct. 2013.
- [20] D. E. Hack, L. K. Patton, B. Himed, and M. A. Saville, "Detection in passive MIMO radar networks," *IEEE Trans. Signal Process.*, vol. 62, no. 11, pp. 2999–3012, Apr. 2014.
- [21] Y. Ma, G. Zhou, and S. Wang, "WiFi sensing with channel state information: A survey," *ACM CSUR*, vol. 52, no. 3, pp. 1–36, Jun. 2019.
- [22] S. Tan, Y. Ren, J. Yang, and Y. Chen, "Commodity WiFi sensing in ten years: Status, challenges, and opportunities," *IEEE Internet Things J.*, vol. 9, no. 18, pp. 17832–17843, Apr. 2022.
- [23] W. Li, B. Tan, and R. Piechocki, "Passive radar for opportunistic monitoring in e-health applications," *IEEE J. Transl. Eng. Health Med.*, vol. 6, pp. 1–10, Jan. 2018.
- [24] W. Li, M. J. Bocus, C. Tang, R. J. Piechocki, K. Woodbridge, and K. Chetty, "On CSI and passive Wi-Fi radar for opportunistic physical activity recognition," *IEEE TWC*, vol. 21, no. 1, pp. 607–620, Jul. 2021.
- [25] T. Martelli, F. Colone, E. Tilli, and A. D. Lallo, "Multi-frequency target detection techniques for DVB-T based passive radar sensors," *Sensors*, vol. 16, no. 10, p. 1594, Sep. 2016.
- [26] A. Ksieeyk et al., "Opportunities and limitations in radar sensing based on 5G broadband cellular networks," *IEEE Aerosp. Electron. Syst. Mag.*, vol. 38, no. 9, pp. 4–21, Apr. 2023.
- [27] P. Samczyński et al., "5G network-based passive radar," *IEEE Trans. Geosci. Remote Sens.*, vol. 60, pp. 1–9, Dec. 2021.
- [28] B. Liu, X. Lyu, and W. Fan, "Analysis of 5G signal for radar application," in *J. Phys. Conf. Ser.*, vol. 2356, no. 1, Oct. 2022, p. 012027.
- [29] P. Lingadevaru, B. Pardhasaradhi, P. Srihari, and G. Sharma, "Analysis of 5G new radio waveform as an illuminator of opportunity for passive bistatic radar," in *2021 IEEE NCC*, 2021, pp. 1–6.
- [30] M. L. Rahman, J. A. Zhang, X. Huang, Y. J. Guo, and R. W. Heath, "Framework for a perceptive mobile network using joint communication and radar sensing," *IEEE Aerosp. Electron. Syst. Mag.*, vol. 56, no. 3, pp. 1926–1941, Sep. 2019.
- [31] C. Sturm, M. Braun, T. Zwick, and W. Wiesbeck, "A multiple target doppler estimation algorithm for OFDM based intelligent radar systems," in *7th IEEE EuRAD*, 2010, pp. 73–76.
- [32] M. Braun, C. Sturm, and F. K. Jondral, "Maximum likelihood speed and distance estimation for OFDM radar," in *2010 IEEE Radar Conf.*, pp. 256–261.
- [33] L. Reichardt, C. Sturm, F. Grünhaupt, and T. Zwick, "Demonstrating the use of the IEEE 802.11p car-to-car communication standard for automotive radar," in *6th IEEE EuCAP*, 2012, pp. 1576–1580.
- [34] B. Kihei, J. A. Copeland, and Y. Chang, "Design considerations for vehicle-to-vehicle IEEE 802.11p radar in collision avoidance," in *2015 IEEE GLOBECOM*, pp. 1–7.



- [35] R. Daniels, E. Yeh, and R. Heath, "Forward collision vehicular radar with IEEE 802.11: Feasibility demonstration through measurements," *IEEE Trans. Veh. Technol.*, vol. 67, no. 2, pp. 1404–1416, Oct. 2018.
- [36] P. Kumari, J. Choi, N. González-Prelcic, and R. W. Heath, "IEEE 802.11ad-based radar: An approach to joint vehicular communication-radar system," *IEEE Trans. Veh. Technol.*, vol. 67, no. 4, pp. 3012–3027, Nov. 2018.
- [37] P. Kumari, D. H. Nguyen, and R. W. Heath, "Performance trade-off in an adaptive IEEE 802.11 ad waveform design for a joint automotive radar and communication system," in *42nd IEEE ICASSP*, 2017, pp. 4281–4285.
- [38] E. Grossi, M. Lops, L. Venturino, and A. Zappone, "Opportunistic radar in IEEE 802.11 ad networks," *IEEE Trans. Signal Process.*, vol. 66, no. 9, pp. 2441–2454, Mar. 2018.
- [39] A. Evers and J. A. Jackson, "Analysis of an LTE waveform for radar applications," in *2014 IEEE Radar Conf.*, 2014, pp. 0200–0205.
- [40] C. B. Barneto, L. Anttila, M. Fleischer, and M. Valkama, "OFDM radar with LTE waveform: Processing and performance," in *2019 IEEE RWS*, pp. 1–4.
- [41] Y. Dan, X. Wan, J. Yi, and Y. Rao, "Ambiguity function analysis of long term evolution transmission for passive radar," in *12th IEEE ISAPE*, 2018, pp. 1–4.
- [42] Y. Cui, X. Jing, and J. Mu, "Integrated sensing and communications via 5G NR waveform: Performance analysis," in *IEEE 2022 ICASSP*, pp. 8747–8751.
- [43] C. Barneto *et al.*, "Radio-based sensing and indoor mapping with millimeter-wave 5G NR signals," in *2020 IEEE ICL-GNSS*, pp. 1–5.
- [44] C. B. Barneto *et al.*, "Full-duplex OFDM radar with LTE and 5G NR waveforms: Challenges, solutions, and measurements," *IEEE Trans. Microw. Theory Tech.*, vol. 67, no. 10, pp. 4042–4054, Aug. 2019.
- [45] Z. Wei *et al.*, "5G PRS-based sensing: A sensing reference signal approach for joint sensing and communication system," *IEEE Trans. Veh. Technol.*, vol. 72, no. 3, pp. 3250–3263, Oct. 2022.
- [46] M. L. Rahman, J. A. Zhang, X. Huang, Y. J. Guo, and Z. Lu, "Joint communication and radar sensing in 5G mobile network by compressive sensing," *IET Commun.*, vol. 14, no. 22, pp. 3977–3988, Dec. 2020.
- [47] O. Kanhere, S. Goyal, M. Beluri, and T. S. Rappaport, "Target localization using bistatic and multistatic radar with 5G NR waveform," in *2021 IEEE VTC2021-Spring*, 2021, pp. 1–7.
- [48] K. M. Braun, "OFDM radar algorithms in mobile communication networks," Ph.D. dissertation, Karlsruhe, Karlsruher Institut für Technologie, 2014.
- [49] K. Qian, C. Wu, Y. Zhang, G. Zhang, Z. Yang, and Y. Liu, "Widar2.0: Passive human tracking with a single wi-fi link," in *Proceedings of the Annual International Conference on Mobile Systems, Applications, and Services (MobiSys)*, 2018, pp. 350–361.
- [50] S. Li, Z. Liu, Y. Zhang, Q. Lv, X. Niu, L. Wang, and D. Zhang, "Wiborder: Precise wi-fi based boundary sensing via through-wall discrimination," *Proceedings of the ACM on Interactive, Mobile, Wearable and Ubiquitous Technologies*, vol. 4, 09 2020.
- [51] Z. Ni, J. A. Zhang, X. Huang, K. Yang, and J. Yuan, "Uplink sensing in perceptive mobile networks with asynchronous transceivers," *IEEE Transactions on Signal Processing*, vol. 69, pp. 1287–1300, 2021.
- [52] Y. Zeng, D. Wu, J. Xiong, E. Yi, R. Gao, and D. Zhang, "Farsense," *Proceedings of the ACM on Interactive, Mobile, Wearable and Ubiquitous Technologies*, vol. 3, pp. 1 – 26, 2019. [Online]. Available: <https://api.semanticscholar.org/CorpusID:195848260>
- [53] Y. Zeng, D. Wu, J. Xiong, J. Liu, Z. Liu, and D. Zhang, "Multisense: Enabling multi-person respiration sensing with commodity wifi," *Proceedings of the ACM on Interactive, Mobile, Wearable and Ubiquitous Technologies*, vol. 4, 09 2020.
- [54] J. Pegoraro, J. O. Lacruz, T. Azzino, M. Mezzavilla, M. Rossi, J. Widmer, and S. Rangan, "Jump: Joint communication and sensing with unsynchronized transceivers made practical," *IEEE Transactions on Wireless Communications*, 2024.
- [55] H. G. Feichtinger, K. Grochenig, and T. Strohmer, "Efficient numerical methods in non-uniform sampling theory," *Numerische Mathematik*, vol. 69, pp. 423–440, Feb. 1995.
- [56] W. H. Press, S. A. Teukolsky, W. T. Vetterling, and B. P. Flannery, *Numerical Recipes 3rd Edition: The Art of Scientific Computing*, 3rd ed. USA: Cambridge University Press, 2007.
- [57] R. Zhang, B. Shim, W. Yuan, M. Di Renzo, X. Dang, and W. Wu, "Integrated sensing and communication waveform design with sparse vector coding: Low sidelobes and ultra reliability," *IEEE Transactions on Vehicular Technology*, vol. 71, no. 4, pp. 4489–4494, 2022.
- [58] W. Zhou, R. Zhang, G. Chen, and W. Wu, "Integrated sensing and communication waveform design: A survey," *IEEE Open Journal of the Communications Society*, vol. 3, pp. 1930–1949, 2022.
- [59] Y. Lo, "A mathematical theory of antenna arrays with randomly spaced elements," *IEEE Trans. Antennas Propag.*, vol. 12, no. 3, pp. 257–268, May 1964.
- [60] D. G. Leeper, "Isophoric arrays-massively thinned phased arrays with well-controlled sidelobes," *IEEE Trans. Antennas Propag.*, vol. 47, no. 12, pp. 1825–1835, Dec. 1999.
- [61] D. Rife and R. Boorstyn, "Single tone parameter estimation from discrete-time observations," *IEEE Trans. Inf. Theory*, vol. 20, no. 5, pp. 591–598, Sep. 1974.
- [62] R. A. Iltis and S. Kim, "Geometric derivation of expectation-maximization and generalized successive interference cancellation algorithms with applications to CDMA channel estimation," *IEEE Trans. Signal Process.*, vol. 51, no. 5, pp. 1367–1377, 2003.
- [63] J. Gansman, J. Krogmeier, and M. Fitz, "Single frequency estimation with non-uniform sampling," in *IEEE ACSSC*, vol. 1, 1996, pp. 399–403.
- [64] M. Braun, C. Sturm, and F. K. Jondral, "On the single-target accuracy of OFDM radar algorithms," in *22nd IEEE PIMRC*, 2011, pp. 794–798.
- [65] B. Fleury, P. Jourdan, and A. Stucki, "High-resolution channel parameter estimation for MIMO applications using the SAGE algorithm," in *2002 Int. Zurich Sem. on Broadband Commun. Access-Transm.-Netw.*, pp. 30–30.
- [66] Martinez-Ingles *et al.*, "Deterministic and experimental indoor mmW channel modeling," *IEEE Antennas Wirel. Propag. Lett.*, vol. 13, pp. 1047–1050, 2014.
- [67] R. Zhang, L. Cheng, S. Wang, Y. Lou, Y. Gao, W. Wu, and D. W. K. Ng, "Integrated sensing and communication with massive mimo: A unified tensor approach for channel and target parameter estimation," *IEEE Transactions on Wireless Communications*, 2024.
- [68] G. P. Blasone, F. Colone, P. Lombardo, P. Wojaczek, and D. Cristallini, "Passive radar dpca schemes with adaptive channel calibration," *IEEE Transactions on Aerospace and Electronic Systems*, vol. 56, no. 5, pp. 4014–4034, 2020.
- [69] J. R. Guerci, *Space-time adaptive processing for radar*. Artech House, 2014.
- [70] X. Gao, S. Roy, and L. Zhang, "Static background removal in vehicular radar: Filtering in azimuth-elevation-doppler domain," 2023. [Online]. Available: <https://arxiv.org/abs/2307.01444>
- [71] C. B. Barneto, T. Riihonen, S. D. Liyanaarachchi, M. Heino, N. González-Prelcic, and M. Valkama, "Beamformer design and optimization for joint communication and full-duplex sensing at mm-waves," *IEEE Transactions on Communications*, vol. 70, no. 12, pp. 8298–8312, 2022.
- [72] R. Wang *et al.*, "A real-time MIMO channel sounder for vehicle-to-vehicle propagation channel at 5.9 GHz," in *2017 IEEE ICC*, pp. 1–6.

**Nikhil K. Nataraja** received the M.S. degree (Hons.) in Electrical Engineering from University of Southern California (USC), Los Angeles, USA in 2022. He is currently pursuing his Ph.D. at USC.

**Sudhanshu Sharma** received the M.S. degree in Electrical Engineering from University of Southern California (USC), Los Angeles, USA. He is currently a Firmware Engineer at Apple Inc.

**Kamran Ali** is a Senior R&D Scientist at General Motors. He graduated with a Ph.D. in Computer Science and Engineering from Michigan State University, USA.

**Dr. Fan Bai** (Member 2005, Sr. Member 2015, Fellow 2016) is a Technical Fellow in the Connected Vehicle Experience Research Lab, Global Research Development, General Motors. He is an IEEE Fellow and an ACM Distinguished Member.

**Rui Wang** received the M.S. degree (Hons.) in 2012, and the Doctorate degree in Electrical Engineering in 2018 from the University of Southern California, Los Angeles, CA, USA. He is currently a software engineer at Google, Mountain View, CA, USA.

**Andreas F. Molisch** is the Golomb-Viterbi Chair professor at the University of Southern California (USC) in Los Angeles, CA. His research interests focus on wireless communications. He is a Fellow of NAI, AAAS, IEEE, IET, URSI, AAIA, and Member of the Austrian Academy of Sciences, and recipient of multiple awards.